International Journal of Nanomedicine

Dovepress
Taylor & Francis Group

Open Access Full Text Article

ORIGINAL RESEARCH

A Multifunctional MIL-101-NH_2(Fe) Nanoplatform for Synergistic Melanoma Therapy

Jinlu Shang[1,2,*], Yongjun Chen[2,*], Fangliang Wang[3,*], Jing Yang[2], Yi Li[4], Liuxuan Yang[2], Xiuqiong Liu[1], Zhirong Zhong[5], Chaochi Yue[6], Meiling Zhou[2]

[1]Department of Pharmacy, West China Hospital Sichuan University Jintang Hospital, Chengdu, Sichuan, 610400, People's Republic of China; [2]Department of Pharmacy, The Affiliated Hospital, Southwest Medical University, Luzhou, Sichuan, 646000, People's Republic of China; [3]Chongqing Key Laboratory for Pharmaceutical Metabolism Research, Chongqing Pharmacodynamic Evaluation Engineering Technology Research Center, College of Pharmacy Chongqing Medical University, Chongqing, 400016, People's Republic of China; [4]Department of Nuclear Medicine, The Affiliated Hospital, Southwest Medical University, Luzhou, Sichuan, 646000, People's Republic of China; [5]Department of Pharmaceutical Sciences, School of Pharmacy, Southwest Medical University, Luzhou, Sichuan, 646000, People's Republic of China; [6]Department of Traditional Chinese Medicine, The Affiliated Hospital, Southwest Medical University, Luzhou, Sichuan, 646000, People's Republic of China

*These authors contributed equally to this work

Correspondence: Meiling Zhou; Chaochi Yue, Email meilzhou@163.com; yuechaochi18@swmu.edu.cn

Background: Melanoma is an aggressive form of skin cancer, and single-modality treatments often fail to prevent tumor recurrence and metastasis. Combination therapy has emerged as an effective approach to improve treatment outcomes.

Methods: In this study, we developed a multifunctional nanoplatform, MIL@DOX@ICG, utilizing MIL-101-NH_2(Fe) as a carrier to co-deliver the chemotherapeutic agent doxorubicin (DOX) and the photosensitizer indocyanine green (ICG). MIL-101-NH_2(Fe) was synthesized via a hydrothermal method. Drug release was evaluated under different pH conditions, and the photothermal effect was tested under near-infrared (NIR) laser irradiation. Hydroxyl radical and reactive oxygen species generation capacities were quantified. Cellular studies using B16F10 cells assessed cytotoxicity, cellular uptake, migration inhibition, and colony formation suppression. In vivo experiments in melanoma-bearing mice evaluated antitumor efficacy and systemic safety through tumor growth inhibition, histological analyses, and toxicity assessments.

Results: MIL@DOX@ICG exhibited a uniform octahedral structure with a particle size of approximately 139 nm and high drug loading efficiencies for DOX (33.70%) and ICG (30.59%). The nanoplatform demonstrated pH-responsive drug release and potent photothermal effects. The generation of hydroxyl radicals via the Fenton reaction and reactive oxygen species production under NIR laser irradiation by MIL@DOX@ICG were confirmed. In vitro assessments revealed significant cytotoxicity of MIL@DOX@ICG against B16F10 cells under NIR laser irradiation, with improved efficacy in inhibiting cell proliferation and migration. In vivo studies confirmed the superior antitumor efficacy of MIL@DOX@ICG + NIR treatment, synergistically harnessing chemotherapy, photothermal therapy, photodynamic therapy, and chemodynamic therapy effects while maintaining excellent biocompatibility.

Conclusion: Our findings underscore the potential of MIL-101-NH_2(Fe) nanoparticles as a versatile and effective platform for synergistic melanoma therapy, offering a promising strategy for overcoming the limitations of conventional treatment modalities.

Keywords: melanoma, MIL-101-NH_2(Fe), chemotherapy, photothermal therapy, photodynamic therapy, chemodynamic therapy

Introduction

Malignant melanoma is characterized by its high aggressiveness and resistance to therapy, representing the leading cause of death among skin cancer patients.[1,2] Currently, the predominant modality for melanoma treatment involves surgical resection. Nevertheless, the presence of residual tumor cells post-surgery frequently leads to tumor recurrence and metastasis.[3] Conventional therapeutic approaches, such as radiotherapy and chemotherapy, face challenges in achieving satisfactory outcomes in melanoma management. Moreover, the adverse effects associated with chemotherapeutic agents limit their clinical benefits.[4] Consequently, there is an urgent need to develop innovative therapeutic strategies aimed at improving the efficacy of melanoma treatment and reducing patient mortality.

Received: 21 October 2024
Accepted: 13 January 2025
Published: 22 January 2025

In recent years, the advent of emerging treatment technologies such as immunotherapy, gene therapy, magnetic therapy, sonodynamic therapy, chemodynamic therapy (CDT), photothermal therapy (PTT), and photodynamic therapy (PDT) have demonstrated considerable promise in the field of cancer treatment.[5–7] Specifically, CDT involves the conversion of overexpressed hydrogen peroxide (H_2O_2) in the tumor microenvironment (TME) into harmful reactive oxygen species (ROS) like hydroxyl radicals (•OH), inducing tumor cell death through apoptosis and necrosis pathways.[8,9] PTT utilizes photothermal agents to rapidly produce heat upon exposure to near-infrared (NIR) laser irradiation, causing irreversible damage to cells through elevated temperature.[10,11] PDT employs specific wavelength light sources to irradiate and excite photosensitizers, leading to the production of cytotoxic ROS, thereby effectively eliminating tumor cells.[12,13] However, the unique physiological characteristics of the TME, such as vascular abnormalities, hypoxia, low pH, and elevated levels of glutathione (GSH) and H_2O_2, pose challenges for achieving significant therapeutic effects using single-modality treatments.[14] To address this issue, the combination of different therapeutic strategies has gained attention as an effective approach.[15–17]

Indocyanine green (ICG) is an FDA-approved fluorescence dye with exceptional properties, including robust NIR absorption and high photothermal conversion efficiency, rendering it suitable for both PTT and PDT.[18,19] However, the application of ICG faces challenges such as instability in aqueous solutions and limited photostability.[20,21] Therefore, enhancing the stability of ICG during PDT and PTT procedures becomes crucial. On the other hand, Doxorubicin (DOX), another FDA-approved chemotherapeutic agent known for its therapeutic efficacy, often induces severe adverse effects and multidrug resistance, significantly reducing its clinical effectiveness.[22] To overcome these issues and improve therapeutic effectiveness, targeted synergistic therapy emerges as a promising strategy.[23]

Combination therapies employing multifunctional nanomaterials have garnered significant attention in recent years.[24,25] Metal-organic frameworks (MOFs), a category of nanoscale porous materials formed through the self-assembly of metal ions and organic ligand molecules, are notable for their distinctive features such as expansive surface areas, uniform porous structures, tunable pore sizes and frameworks, and biodegradable nature.[26,27] These properties have facilitated widespread application in areas including gas adsorption and separation, catalysis, electrochemical biosensing, and drug delivery.[28–30] Among these, the iron-based MOF, MIL-101-NH_2(Fe), has attracted considerable interest due to its high drug loading capacity, favorable stability, and low biological toxicity.[31,32] Recent investigations have demonstrated that MIL-101-NH_2(Fe) can induce protective autophagy in normal cells while inducing ferroptosis in cancer cells. When employed as carriers in nano drug delivery systems, MIL-101-NH_2(Fe) capitalizes on the enhanced permeability and retention effect within tumor microvessels, enabling the selective targeting of tumor tissues.[33,34] Moreover, it exhibits a pronounced response to the weak acidity of the TME, enabling controlled drug release and achieving tumor accumulation.[35] Furthermore, the Fe^{3+} in MIL-101-NH_2(Fe) can trigger a Fenton reaction in the presence of GSH and H_2O_2 within the TME, resulting in the generation of ROS and inducing a CDT effect, thus further amplifying therapeutic outcomes.[36]

In this study, we successfully synthesized MIL-101-NH_2(Fe) and co-loaded it with the chemotherapeutic agent DOX and the photosensitizer ICG, resulting in the development of a novel multifunctional integrated treatment system termed MIL@DOX@ICG. This innovative system was employed to achieve a combination therapy involving chemotherapy, PTT, PDT, and CDT. Comprehensive analyses were performed to characterize the morphology, particle size, zeta potential, encapsulation efficiency (EE), and drug loading capacity (DL) of MIL@DOX@ICG. Furthermore, we investigated the drug release behavior of MIL@DOX@ICG under varying pH conditions, its photothermal conversion efficiency, and its capacity to generate •OH and ROS. The cytotoxicity, cellular uptake, anti-migratory effects, and inhibition of clonal proliferation of MIL@DOX@ICG upon NIR laser irradiation were assessed in B16F10 cells. Additionally, a mouse melanoma model was established to evaluate the synergistic antitumor efficacy and safety profile of MIL@DOX@ICG under NIR laser exposure. This study not only introduces a novel therapeutic approach for melanoma treatment but also underscores the great potential of multifunctional nanomaterials in the realm of combination treatment strategies.

Materials and Methods

Materials

Ferric chloride hexahydrate ($FeCl_3 \cdot 6H_2O$), 3.3′,5,5′-tetramethylbenzidine (TMB), and 1.3-diphenylisobenzofuran (DPBF) were acquired from Macklin Biochemical Technology (Shanghai, China). 2-Aminoterephthalic acid was sourced from Aladdin Biochemical Technology (Shanghai, China). DOX was obtained from Dibai Biotechnology (Shanghai, China). ICG was procured from Jizhi Biochemical Technology (Shanghai, China). The ROS detection kit was provided by Biyuntian Biotechnology (Shanghai, China). The TUNEL assay kit and Ki67 antibody were purchased from Sevier Biotechnology (Wuhan, China).

B16F10 cells were purchased from Fenghui Biotechnology (Hunan, China). Male C57BL/6J mice, aged 6–8 weeks old and weighing 20–22 g, were sourced from Hua Fukang Biological Technology (Beijing, China). All procedures involving animals were conducted in accordance with the National Research Council's Guide for the Care and Use of Laboratory Animals and were approved by the Animal Ethics Committee of Southwest Medical University (approval number: 20231113-006).

Preparation and Characterization of MIL@DOX@ICG

$FeCl_3 \cdot 6H_2O$ (81.1 mg) and 2-aminoterephthalic acid (54.3 mg) were dissolved in 20 mL of dimethylformamide and added with 200 μL of glacial acetic acid. The resulting mixture underwent sonication for 30 min, then transferred to a 25 mL autoclave for reaction at 120 °C for 24 h. Subsequently, the reaction solution was centrifuged at 20,000 × g for 10 min, and the precipitate was washed thrice with dimethylformamide and ethanol, respectively. The final product was dried under vacuum to yield the MIL-101-NH_2(Fe).

DOX (10 mg) and ICG (10 mg) were dissolved in 10 mL of absolute ethanol. Subsequently, 10 mg of MIL-101-NH_2 (Fe), previously activated under vacuum at 100 °C for 2 h, was introduced into the dispersion, and the resulting mixture was stirred for 24 h. The reaction solution was centrifuged, followed by three washes with pure water. The supernatant was analyzed to determine the concentrations of free DOX and ICG, and the EE and DL were calculated. The resulting precipitate was freeze-dried to yield MIL@DOX@ICG. MIL@DOX and MIL@ICG were prepared in the same method.

The morphology of the nanoparticles was assessed using a scanning electron microscope (SEM) (Zeiss, Germany), with particle size determined through Image J software. Zeta potential measurements were conducted with a laser particle size analyzer (Malvern, UK). The absorption spectra of the samples in the ultraviolet-visible (UV-Vis) range (200–900 nm) were recorded using a UV-Vis spectrophotometer (Beijing Purkinje General Instrument, China). Fourier transform infrared (FTIR) spectra were obtained over the range of 4000 to 400 cm^{-1} using an FTIR spectrometer (Thermo Fisher, USA).

Drug Release and Stability Studies

Specified quantities of free drugs and nanoparticles were dispersed in 3 mL of release medium and sealed within separate dialysis bags. Subsequently, these bags were immersed into brown bottles containing 100 mL medium at varying pH levels (5.5, 6.5, 7.4) and incubated on a constant temperature shaker at 37 °C with 50 rpm. At designated intervals, 1 mL of the external solution was withdrawn and replaced with an equivalent volume of fresh medium. The absorbance of DOX and ICG in the samples was determined, and the cumulative release rate was calculated.

For photothermal stability assessment, a 250 μg/mL solution of MIL@DOX@ICG was irradiated with an 808 nm laser (2 W/cm^2 for 11 min) on days 1, 2, 3, 4, 5, 7, and 9 to evaluate the photothermal effect. Additionally, the zeta potential of MIL@DOX@ICG in PBS and PBS containing 10% fetal bovine serum (FBS) was measured using a laser particle size analyzer over a 7-day period to assess the stability of the nanoplatform.

•OH Generation Detection

20 μL of DMSO solution containing TMB (20 mM) and 2 μL of H_2O_2 aqueous solution (6 mM) were added to 500 μL of MIL@DOX@ICG solution at 140 μg/mL. Subsequently, the UV-Vis absorption spectra were recorded at 550–700 nm every 90 s. Furthermore, MIL@DOX@ICG solutions at concentrations of 70, 140, 280, and 560 μg/mL were prepared.

 https://doi.org/10.2147/IJN.S502089

For each concentration, 500 μL was taken and added with 20 μL of DMSO solution containing TMB (20 mM) and 2 μL of H_2O_2 aqueous solution (6 mM), with the absorbance at 655 nm detected at 20-s intervals. To examine the impact of varying H_2O_2 concentrations on the generation of •OH, 500 μL of the MIL@DOX@ICG solution (140 μg/mL) was mixed with 20 μL of DMSO solution containing TMB (20 mM) and 2 μL of H_2O_2 aqueous solution at varying concentrations (2, 4, 6, and 8 mM), with absorbance at 655 nm monitored every 20 s. The •OH production capacity of MIL-101-NH_2(Fe) was evaluated under identical conditions.

ROS Generation Detection

20 μL of DMSO solution containing DPBF (20 mM) and 4 μL of H_2O_2 aqueous solution (6 mM) were mixed with 1 mL of ICG or MIL@DOX@ICG solutions. A control group was set up without the addition of H_2O_2. The resulting mixtures were then subjected to irradiation using an 808 nm laser for 0, 1, 3, 5, 7, and 9 min, respectively. The UV-Vis absorption spectra of DPBF were recorded at 300–800 nm employing a microplate reader.

Photothermal Effect of MIL-101@DOX@ICG

To explore the impact of concentration on the photothermal response, MIL@DOX@ICG solutions at different concentrations were subjected to irradiation using an 808 nm laser at 2.0 W/cm^2, with pure water serving as the control. Additionally, to examine the effect of laser power on the photothermal response, 250 μg/mL of MIL@DOX@ICG solution underwent irradiation at various power densities with an 808 nm laser. Temperature changes were monitored using a thermocouple thermometer.

For the photothermal cycling capability investigation, 250 μg/mL of MIL@DOX@ICG solution was exposed to an 808 nm laser for 11 min at 2.0 W/cm^2. Subsequently, the laser was deactivated, allowing the solution to naturally cool to its initial temperature. The laser was then resumed, and the sample underwent another exposure cycle. This irradiation and cooling procedure was repeated five times, based on established protocols in the literature,[37,38] to simulate repeated photothermal treatment sessions typically encountered in practical therapeutic applications. The characteristic thermal time constant was derived from the cooling rate change curve, enabling the calculation of the photothermal conversion efficiency.

Cytotoxicity

The cytotoxicity of free drugs, nanoparticles, and NIR laser irradiation on B16F10 cells was evaluated by the CCK-8 method. B16F10 cells were seeded in 96-well plates, and the culture medium containing different concentrations of the therapeutic agents (DOX concentrations: 0.25 to 4 μg/mL) was added. Groups designated for laser treatment underwent an 808 laser irradiation for 8 min (2 W/cm^2) after 4 h of incubation. After a total incubation period of 48 h, 10 μL of CCK-8 solution was added, and cell viability was determined by measuring the absorbance at 450 nm using a microplate reader.

Cellular Uptake and Mechanism Study

B16F10 cells were seeded on cell climbing slices within 6-well plates. For the dose-dependent experiment, cells were incubated with MIL@DOX@ICG at various concentrations for 8 h. For the time-dependent experiment, cells were exposed to 30 μg/mL of MIL@DOX@ICG and incubated at different times. Subsequently, the cells were stained with Hoechst 33342 and fixed with 4% paraformaldehyde. Cellular uptake was visualized using a confocal laser scanning microscope (CLSM) (Leica, Germany), with fluorescence intensity quantified using Image J software.

To further study the cellular mechanism, B16F10 cells were cultured in 6-well plates with cell climbing slices. In the temperature-dependent uptake study, cells were exposed to 30 μg/mL of MIL@DOX@ICG for 8 h at 37 and 4 °C, respectively. To explore the involvement of different endocytic pathways, cells were pre-incubated for 2 h with specific inhibitors targeting distinct pathways: 10 μg/mL chlorpromazine (CHLO), 50 μg/mL nystatin (NY), and 100 μg/mL amiloride (AMI). Subsequently, the cells were exposed to 30 μg/mL MIL@DOX@ICG for another 8 h. Following staining and fixation, images were captured using CLSM and analyzed with Image J software.

Wound Healing Study

B16F10 cells were seeded in 24-well plates, and straight scratches were created in each well using a sterile pipette tip to simulate wounds. Following this, 1 mL of DOX, ICG, MIL-101-NH_2(Fe), MIL@DOX, MIL@ICG, or MIL@DOX@ICG (DOX concentration: 1 μg/mL) was added, while the control group received a drug-free medium. Groups designated for laser treatment were exposed to an 808 laser for 10 min daily at 2 W/cm^2. At 0 and 36 h after scratch generation, wound closures were recorded using a light microscope. The resulting images were processed using Image J software, and the cell migration percentage was calculated accordingly.

Cell Colony Formation Study

B16F10 cells were seeded in 6-well plates and incubated overnight. 2 mL of DOX, ICG, MIL-101-NH_2(Fe), MIL@DOX, MIL@ICG, or MIL@DOX@ICG (DOX concentration: 0.5 μg/mL) was added, while the control group received 2 mL of drug-free medium. Groups designated for laser treatment were irradiated with an 808 laser for 10 min each day at 2 W/cm^2. After an 8-day incubation period, the cells were fixed and stained with crystal violet. The number of colonies formed was counted to evaluate the proliferative capacity of the cells under different treatment conditions.

Intracellular ROS Generation Assessment

B16F10 cells were cultured in 6-well plates and incubated overnight. MIL-101-NH_2(Fe), ICG, or MIL@DOX@ICG (MIL-101-NH_2(Fe) concentration: 10 μg/mL) were added and incubated for 6 h. Groups designated for NIR laser treatment were exposed to an 808 nm laser irradiation for 15 min at 2 W/cm^2. After incubation, 1 mL of Hoechst 33342 (20 μg/mL) and 1 mL of DCFH-DA (10 μM) were added and incubated for 30 min. After fixation, images were captured using CLSM and analyzed using Image J software.

In vivo Antitumor and Safety Assessment

B16F10 cells (1×10^6) were subcutaneously inoculated into the backs of C57BL/6J mice to establish a melanoma-bearing mouse model. Once tumor volumes reached around 100 mm^3 (defined as day 1), the mice were randomly allocated into ten groups: PBS, MIL-101-NH_2(Fe), ICG, ICG + NIR, DOX, MIL@ICG, MIL@ICG + NIR, MIL@DOX, MIL@DOX@ICG, and MIL@DOX@ICG + NIR, with 5 animals in each group. On days 1, 4, and 7, mice received intratumoral injections of 100 μL of PBS or the respective therapeutic agents (DOX concentration: 2.5 mg/kg). For groups undergoing NIR laser treatment, mice were anesthetized after administration, and their tumor sites were irradiated with an NIR laser for 5 min at 0.5 W/cm^2. Temperature changes were recorded before and every min after irradiation. During the treatment period, the body weights of the mice were monitored every two days. On day 8, the mice were sacrificed, and the tumors were excised and weighed. The tumor samples were then fixed with 4% paraformaldehyde, embedded in paraffin, and serially sectioned. Histopathological analysis was performed by H&E staining, and tumor cell proliferation and apoptosis were assessed using Ki67 immunostaining and TUNEL assay, respectively.

To further assess in vivo safety, blood samples were collected from each group for routine blood analysis before the mice were sacrificed on day 8. Mouse whole blood was collected using centrifuge tubes containing EDTA-K2, and hematological parameters were detected by a hematology analyzer (BC-6000Plus, Mindray). Following euthanasia, the major organs were excised from each group, washed with 0.9% saline, dried with filter paper, and weighed. Organ-to-body and organ-to-brain weight ratios were then calculated to evaluate systemic toxicity.

Statistical Analysis

Statistical analyses were conducted using GraphPad Prism 9.0 software. The Student's *t*-test was utilized to evaluate differences between the two groups, while a one-way analysis of variance was employed for comparisons among multiple groups. A significance threshold of $P < 0.05$ was applied to determine statistical significance.

Results and Discussion

Preparation and Characterization of MIL@DOX@ICG

MIL-101-NH_2(Fe) was synthesized utilizing a hydrothermal method, as described in previous literature.[39,40] SEM analysis revealed a well-defined octahedral structure of MIL-101-NH_2(Fe), aligning with prior reports (Figure 1A).[39,40] After drug encapsulation, the nanoparticles retained their uniform size and regular octahedral morphology, with a slight increase in particle size observed (Figure 1B–D). Specifically, the particle sizes of MIL-101-NH_2(Fe), MIL@DOX, MIL@ICG, and MIL@DOX@ICG were measured at 122.08 ± 29.29, 133.01 ± 29.43, 132 ± 22.82, and 139.42 ± 30.16 nm, respectively (Figure 1E–H).

As summarized in Table S1, the EE and DL of DOX in MIL@DOX@ICG were 94.69 ± 0.74% and 33.70 ± 0.78%, respectively. Similarly, the EE and DL of ICG in MIL@DOX@ICG were determined to be 85.05 ± 5.45% and 30.59 ± 1.41%, respectively. In contrast, other drug delivery systems co-loading DOX and ICG demonstrate significantly lower drug loading capacities. For instance, a folate-receptor-targeted liposome system (FA-DOX-ICG-PFP@Lip) reported DOX and ICG drug loading contents of only 6.20 ± 0.51% and 9.19 ± 0.29%, respectively.[19] Similarly, a poly(lactic-co-glycolic acid)-based nanoparticle system (PSC/ICG@+DOX) achieved DOX and ICG loading contents of just 6.79% and 2.57%, respectively.[6] The notably high drug loading efficiencies of MIL@DOX@ICG underscore the robust affinity and capability of MIL-101-NH_2(Fe) for the stable encapsulation of therapeutic agents, essential for delivering sufficient drug concentrations to the tumor site to achieve desired therapeutic outcomes. Additionally, the zeta potential of MIL-101-NH_2(Fe) was measured at −3.97 ± 0.52 mV (Figure 1I). Upon DOX loading, the zeta potential shifted to a positive charge, measuring at 8.26 ± 0.25 mV, which is attributed to the amino groups on the surface of DOX. Conversely, due to the abundant negative sulfate groups on the surface of ICG, MIL@ICG exhibited a negative charge of −27.6 ± 2.98 mV. After the co-loading of DOX and ICG, the zeta potential of MIL@DOX@ICG was recorded at −10.65 ± 2.05 mV.

As presented in Figure 1J, the characteristic absorption peaks of free DOX were observed at 233 and 480 nm, while both MIL@DOX and MIL@DOX@ICG displayed analogous absorption peaks at these same wavelengths, confirming the successful encapsulation of DOX. Similarly, free ICG exhibited a characteristic absorption peak at 787 nm, with both MIL@ICG and MIL@DOX@ICG displaying analogous absorption peaks, indicating the successful loading of ICG.

In the FTIR spectra (Figure 1K), the peak at 3375 cm^{-1} in MIL-101-NH_2(Fe) corresponded to the stretching vibration of the N-H bond, while peaks at 1655 and 1581 cm^{-1} were attributed to the C=O and C=N bonds, respectively. Additionally, the peak at 770 cm^{-1} was caused by the stretching vibration of the O-Fe-O bond. In the FTIR spectrum of DOX, peaks at 1728 and 1618 cm^{-1} were observed, corresponding to the N-H and CO-H bonds, respectively. ICG exhibited a characteristic vinyl peak at 1087 cm^{-1}. Further analysis revealed that MIL@DOX retained the characteristic peaks of DOX at 1728 and 1619 cm^{-1}, indicating the successful loading of DOX. Similarly, MIL@ICG displayed the vinyl characteristic peak of ICG at 1094 cm^{-1}, confirming successful ICG encapsulation. Notably, all characteristic peaks observed in MIL-101-NH_2(Fe), DOX, and ICG were presented in the FTIR spectra of MIL@DOX@ICG, providing further evidence for the successful preparation of MIL@DOX@ICG.

Drug Release and Stability Investigation

The release profiles of nanoparticles under different pH conditions were systematically investigated, along with the release behavior of free DOX and ICG at pH 7.4. As depicted in Figure 2A and B, within 24 h at pH 7.4, approximately 98% of DOX was released from free DOX, while only 37% and 23% were released from MIL@DOX and MIL@DOX@ICG, respectively. Similarly, the release of ICG from free ICG, MIL@ICG, and MIL@DOX@ICG reached about 101%, 30%, and 21%, respectively. These findings underscore the excellent sustained-release properties of the nano-formulations after drug encapsulation within MIL-101-NH_2(Fe). Notably, as the pH value decreased, the drug release rate accelerated. As a pH of 5.5, within 24 h, the release rates of DOX from MIL@DOX and MIL@DOX@ICG rose to 89% and 67%, respectively, and ICG release from MIL@ICG and MIL@DOX@ICG increased to 88% and 72%, respectively. Therefore, the loading of drugs into MIL-101-NH_2(Fe) resulted in pH-responsive release behavior under mildly acidic conditions.

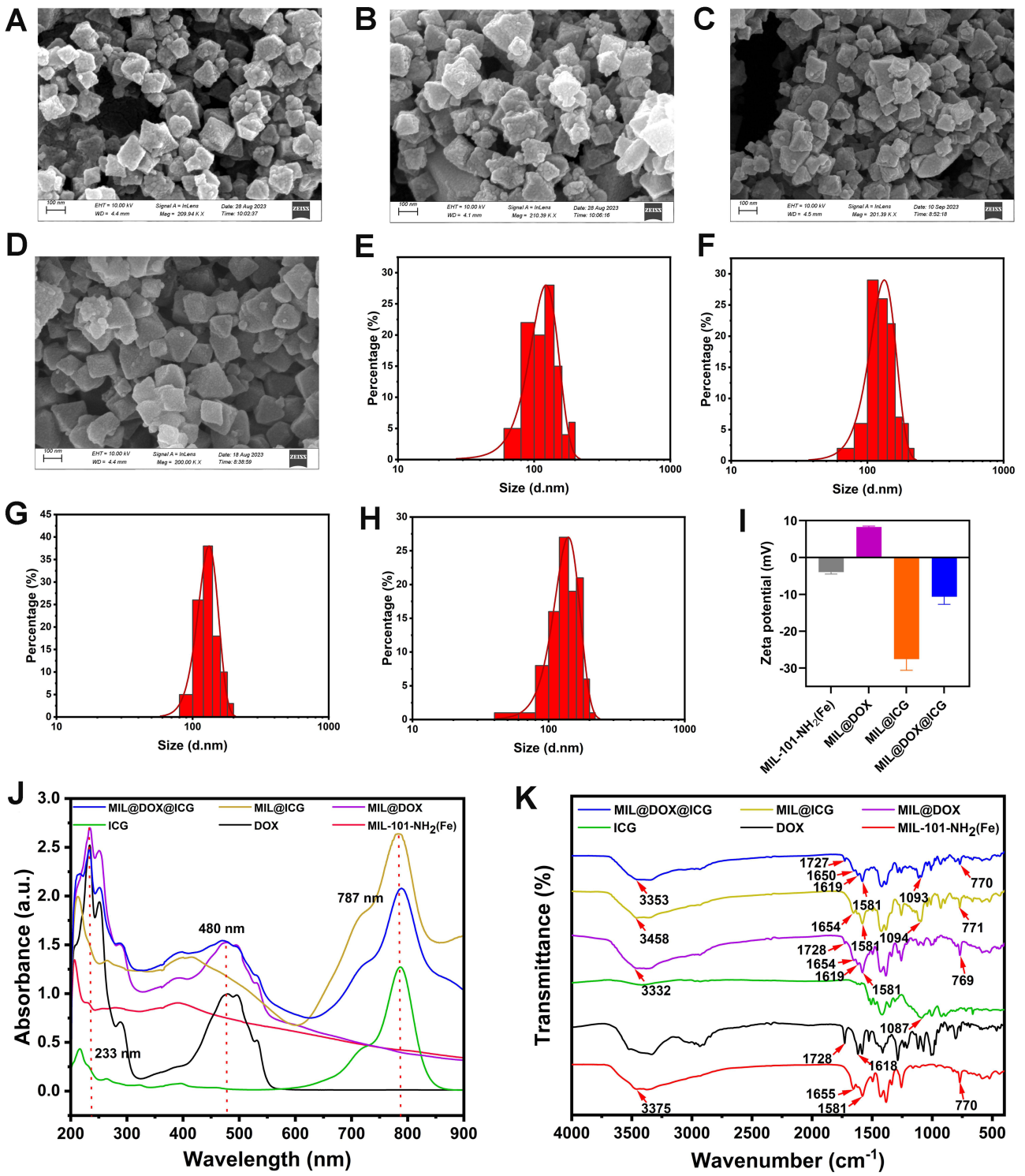

Figure 1 SEM images of (**A**) MIL-101-NH_2(Fe), (**B**) MIL@DOX, (**C**) MIL@ICG, and (**D**) MIL@DOX@ICG, with scale bar = 100 nm. Particle size distribution histograms of (**E**) MIL-101-NH_2(Fe), (**F**) MIL@DOX, (**G**) MIL@ICG, and (**H**) MIL@DOX@ICG. (**I**) Zeta potential detection. (**J**) UV-Vis and (**K**) FTIR spectra of DOX, ICG, MIL-101-NH_2(Fe), MIL@DOX, MIL@ICG, and MIL@DOX@ICG.

The underlying pH-responsive release mechanism is attributed to the unique structural and chemical properties of MIL-101-NH_2(Fe). Under acidic conditions in the TME, the metal nodes of MIL-101-NH_2(Fe) may undergo reactions that lead to partial disintegration or alterations in porosity, thereby facilitating drug release. Acidic conditions may also weaken the electrostatic interactions or hydrogen bonds between the drugs and MIL-101-NH_2(Fe), effectively promoting

https://doi.org/10.2147/IJN.S502089

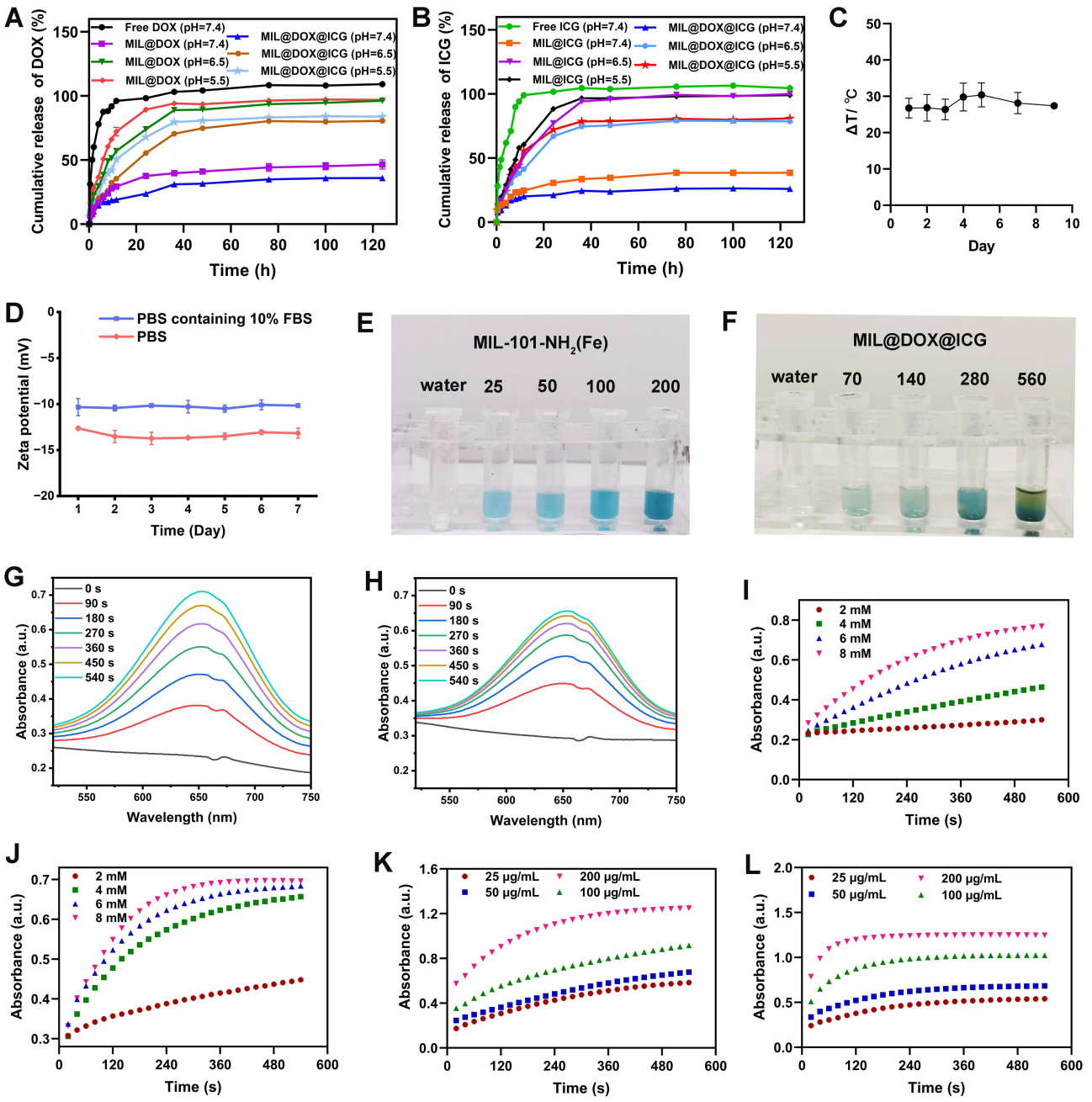

Figure 2 (**A** and **B**) Cumulative release curves of DOX, ICG, MIL@DOX, MIL@ICG, and MIL@DOX@ICG at various pH levels. (**C**) Stability of MIL@DOX@ICG through photothermal effect testing. (**D**) Zeta potential stability of MIL@DOX@ICG in PBS and PBS containing 10% FBS. Photographs of the reaction solutions with the addition of different concentrations of (**E**) MIL-101-NH_2(Fe) and (**F**) MIL@DOX@ICG with 6 mm of H_2O_2. Time-dependent UV-Vis spectra of oxTMB with the addition of (**G**) MIL-101-NH_2(Fe) and (**H**) MIL@DOX@ICG (H_2O_2: 6 mm). Time-dependent absorbance changes of oxTMB with the addition of (**I**) MIL-101-NH_2(Fe) and (**J**) MIL@DOX@ICG at different H_2O_2 concentrations (2, 4, 6, and 8 mm). Time-dependent absorbance changes of oxTMB with the addition of different concentrations of (**K**) MIL-101-NH_2(Fe) and (**L**) MIL@DOX@ICG (20, 50, 100, and 200 μg/mL) with 6 mm of H_2O_2.

drug desorption. Furthermore, the protonation of amine groups (-NH_2) on the surface of MIL-101-NH_2(Fe) under these acidic conditions can alter the surface characteristics of the carrier, influencing the adsorption and desorption dynamics of the drugs. Thus, the pH-responsive release mechanism of MIL-101-NH_2(Fe) facilitates controlled and accelerated release of DOX and ICG in the acidic TME, ensuring targeted delivery and accumulation of therapeutic agents at the tumor site.

The inherent instability of ICG has been a significant limitation for its clinical application. To address this, stability assessments were conducted to evaluate the photothermal and zeta potential stability of MIL@DOX@ICG. As shown in

Figure 2C, MIL@DOX@ICG maintained excellent and stable heat production capacity over 9 days, indicating enhanced stability of ICG in the aqueous solution upon loading within MIL-101-NH_2(Fe). Furthermore, the zeta potential of MIL@DOX@ICG exhibited only minor variations in both PBS and PBS supplemented with 10% FBS over 7 days (Figure 2D). The MIL-101-NH_2(Fe) matrix provides a protective environment that prevents aqueous-induced degradation and inhibits self-aggregation of ICG molecules, thereby enhancing the potential of this nano-formulation for photothermal therapy applications. Moreover, encapsulation within MIL-101-NH_2(Fe) can improve the bioavailability and photothermal conversion efficiency of ICG, broadening its clinical applicability.

•OH Generation Detection

Fe^{3+} within MIL-101-NH_2(Fe) can catalyze the conversion of H_2O_2 into highly toxic •OH through the Fenton reaction. To evaluate the catalytic performance of nanoparticles, TMB was utilized as an indicator to detect the generation of •OH. As illustrated in Figure 2E and F, aqueous solutions containing 6 mM H_2O_2 showed no observable color change after adding TMB. However, the introduction of both MIL-101-NH_2(Fe) and MIL@DOX@ICG resulted in the solution turning blue, indicating the oxidation of TMB to its cation radical (oxTMB) by •OH, thereby confirming the •OH generation. With prolonged reaction time, the production of oxTMB increased, as evidenced by the enhanced absorbance at 655 nm (Figure 2G and H) and the darkening of the solution color. Furthermore, the reaction of nanoparticles with varying H_2O_2 concentrations indicated that higher H_2O_2 levels led to increased absorbance at 655 nm (Figure 2I and J). Moreover, as the concentrations of MIL-101-NH_2(Fe) and MIL@DOX@ICG elevated, oxTMB production also increased, indicating enhanced •OH production (Figure 2K and L). The successful detection of •OH generation in the presence of MIL-101-NH_2(Fe) and MIL@DOX@ICG validates the catalytic performance of these nanoparticles, which can enhance the therapeutic efficacy by producing cytotoxic •OH in response to the elevated levels of H_2O_2 within the TME.

ROS Generation Detection

DPBF is a fluorescent probe with high specificity for singlet oxygen ($^1O_2$). Upon interaction with $^1O_2$, DPBF undergoes irreversible oxidation, resulting in a rapid decrease in absorption intensity at 410 nm. As shown in Figure 3A, in the absence of H_2O_2, prolonged irradiation with an 808 nm laser led to increased $^1O_2$ production induced by free ICG, corresponding to a reduction in DPBF absorption. After the addition of H_2O_2, the characteristic absorption of DPBF remained largely unchanged, indicating that H_2O_2 does not significantly influence the induction of $^1O_2$ by free ICG (Figure 3B). Similarly, under NIR laser irradiation, the MIL@DOX@ICG group demonstrated a significant reduction in DPBF absorption, suggesting its capacity to induce $^1O_2$ generation (Figure 3C). Notably, following H_2O_2 addition, the characteristic absorption of DPBF in the MIL@DOX@ICG group underwent a substantial decrease after NIR laser irradiation of equivalent power intensity and duration (Figure 3D). This observation revealed that MIL@DOX@ICG possesses a potent ROS generation capability, facilitated by the generation of •OH from MIL-101-NH_2(Fe) upon H_2O_2 addition, which further oxidized DPBF. The pivotal role of $^1O_2$ in PDT is highlighted by its contribution to oxidative damage within tumor cells. The capacity of MIL@DOX@ICG to generate $^1O_2$ under NIR laser irradiation significantly enhances its application in PDT, highlighting its potential as a multifunctional therapeutic agent.

Photothermal Effect of MIL@DOX@ICG

An 808 nm laser at 2.0 W/cm^2 was utilized to irradiate MIL@DOX@ICG aqueous solutions with different concentrations, and their temperature rise curves were monitored. Concentration-dependent increases in the heat-generating capacity of MIL@DOX@ICG were observed, with the temperature at 1000 μg/mL increasing by 38.6 °C after 11 min of laser irradiation (Figure 3E). Furthermore, elevating the laser power density led to a corresponding enhancement in the photothermal effect of the MIL@DOX@ICG samples (Figure 3F). Infrared thermography images of MIL@DOX@ICG at different concentrations are shown in Figure 3G. Given the known instability of ICG in aqueous environments, an investigation into the photothermal cycling capability of MIL@DOX@ICG was conducted. Impressively, MIL@DOX@ICG retained its robust photothermal activity after undergoing five laser on/off cycles (Figure 3H). According to the cooling rate change curve, the photothermal conversion efficiency of MIL@DOX@ICG was calculated

 https://doi.org/10.2147/IJN.S502089

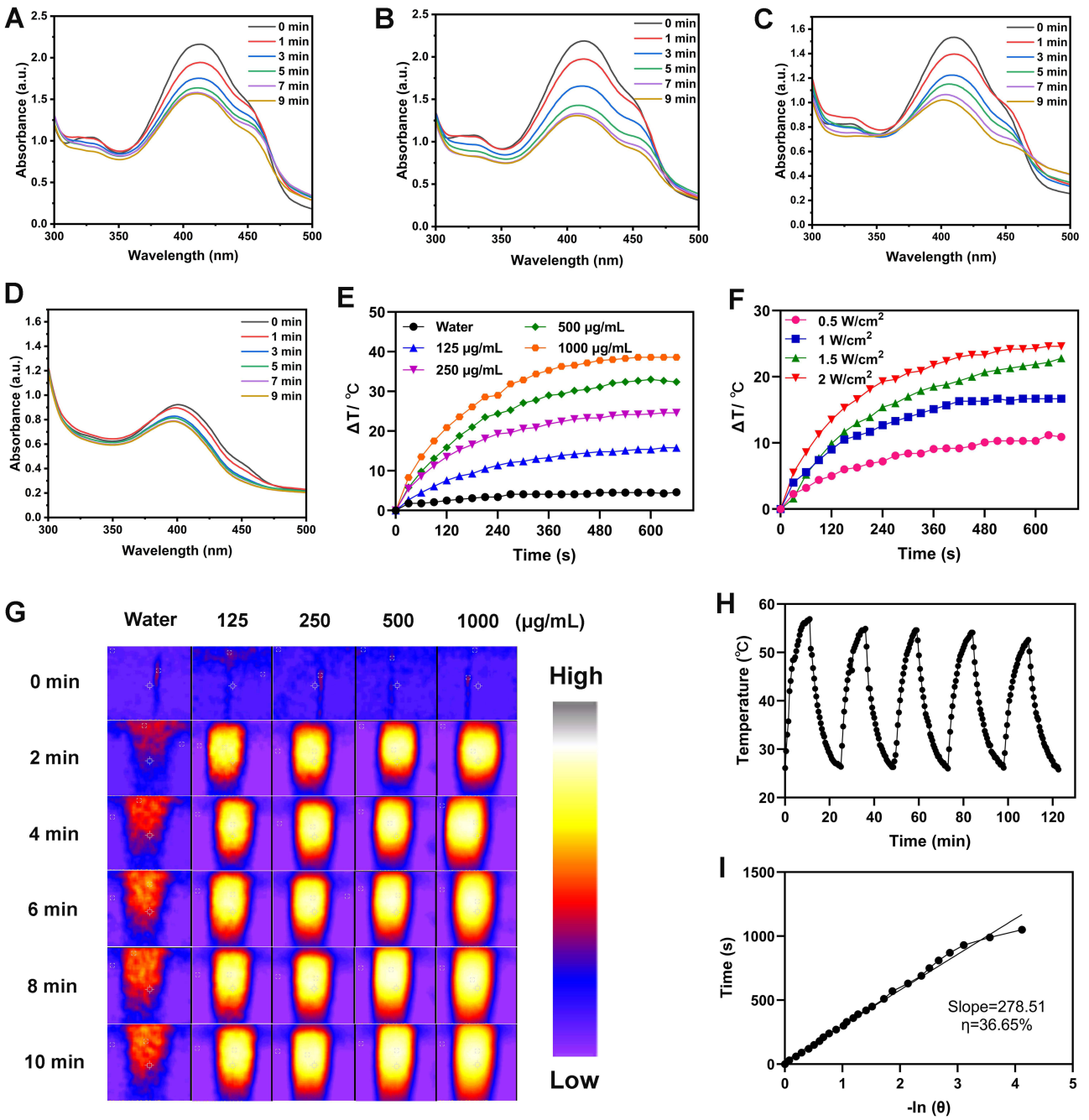

Figure 3 Time-dependent UV-Vis spectra of DPBF with the reaction of ICG (**A**) without H_2O_2 or (**B**) with H_2O_2. Time-dependent UV-Vis spectra of DPBF with the reaction of MIL@DOX@ICG (**C**) without H_2O_2 or (**D**) with H_2O_2. Temperature rising curve of MIL@DOX@ICG (**E**) at different concentrations and (**F**) at different power densities. (**G**) Infrared thermography of MIL@DOX@ICG at different concentrations. (**H**) Photothermal cycle stability of MIL@DOX@ICG. (**I**) Cooling rate change curve of MIL@DOX@ICG.

to be 36.65% (Figure 3I), which significantly exceeds those reported for similar drug delivery systems co-loading DOX and ICG. For instance, a microneedle-based delivery system (D/I@PATC) exhibited a photothermal conversion efficiency of only 17.2%,[2] and a cubosome-based system (DOX-ICG-cubo) achieved 25.16%.[1] These comparatively lower efficiencies demonstrate the advantages of MIL-101-NH_2(Fe) as a nanoplatform for achieving superior photothermal performance.

The potent photothermal effect generated by MIL@DOX@ICG underscores its potential for inducing localized hyperthermia, rendering it suitable for effective PTT against cancer cells. Moreover, the observed enhancement in

photothermal response with increased nanoparticle concentration and laser power density highlights the tunable photothermal properties of MIL@DOX@ICG. This tunability is essential for tailoring PTT to meet specific clinical requirements, allowing precise control over the thermal dose delivered to the tumor site. The photothermal cycling capability of MIL@DOX@ICG is critical for repeated PTT treatments, indicating its potential for long-term applications in cancer therapy, where multiple treatment cycles are often necessary.

Evaluation of Cytotoxicity

Based on the unique responsiveness of MIL@DOX@ICG to the TME, its in vitro antitumor efficacy at the cellular level was studied using a CCK-8 method. The impact of NIR laser irradiation on cell viability was found to be negligible, with cell survival rates remaining above 90% (Figure 4A). MIL-101-NH_2(Fe) exhibited minimal cytotoxicity at low concentrations (0.4–10 μg/mL), maintaining cell survival rates above 80%. However, higher carrier concentrations led to a notable decrease in cell survival rates, possibly due to the elevated Fe^{3+} concentration enhancing the Fenton reaction within tumor cells, consequently increasing ROS levels and exerting a CDT effect to eliminate tumor cells.

Figure 4B indicated that both free ICG and MIL@ICG displayed cell survival rates above 80% at concentrations ranging from 0.25–4 μg/mL, suggesting negligible toxicity to B16F10 cells. However, upon exposure to an 808 nm laser, cell viability significantly decreased with increasing concentrations of ICG and MIL@ICG. At lower concentrations, laser exposure exhibited a limited impact on cell viability, likely due to insufficient photothermal and photodynamic effects resulting from lower ICG concentration. Nonetheless, at concentrations exceeding 1 μg/mL, a substantial decline in cell viability was observed, attributed to the potent photothermal and photodynamic effects of ICG. Notably, at ICG concentrations exceeding 2 μg/mL, the cytotoxicity observed in the ICG + NIR group surpassed that of the MIL@ICG + NIR group, potentially reflecting the sustained release of ICG from the carrier, as validated by drug release experiments, where enhanced photothermal and photodynamic effects may occur upon gradual ICG release.

Following the loading of the chemotherapeutic drug, the MIL@DOX, MIL@DOX@ICG, and MIL@DOX@ICG + NIR groups exhibited concentration-dependent cytotoxic effects (Figure 4C). At 4 μg/mL, the cell survival rate in the MIL@DOX@ICG + NIR group declined to only 2.03%, compared to 6.47%, 23.01%, and 15.48% in the DOX, MIL@DOX, and MIL@DOX@ICG groups, respectively, indicating significantly enhanced cytotoxicity. This enhancement can be attributed to the combination of chemotherapy and the photothermal and photodynamic effects induced by ICG post-laser irradiation. Furthermore, the elevated temperature resulting from the photothermal response accelerated the release of Fe^{3+} and drugs from MIL@DOX@ICG, thereby amplifying the Fenton reaction and chemotherapeutic impact while promoting continuous ROS accumulation. Hence, MIL@DOX@ICG + NIR demonstrated superior cytotoxicity compared to single treatments, achieving synergistic therapeutic effects that integrate chemotherapy, PTT, PDT, and CDT.

Cellular Uptake and Mechanism Study

Efficient internalization and delivery of therapeutic agents into the tumor cytoplasm and nucleus are crucial for successful treatment.[41] CLSM was used to evaluate the concentration- and time-dependent uptake of MIL@DOX@ICG. After incubating B16F10 cells with different concentrations of MIL@DOX@ICG, the nanoparticles penetrated the cells and were predominantly localized within the nucleus. This localization is attributed to the disintegration of MIL@DOX@ICG within the acidic intracellular environment (endosomes/lysosomes), triggering the release of DOX due to its acid-sensitive properties. Subsequently, DOX translocates to the nucleus, accumulating therein and targeting DNA, thereby inhibiting tumor cell division and proliferation.[42] With increasing concentration, the red fluorescence indicative of DOX progressively intensified, demonstrating a concentration-dependent uptake of MIL@DOX@ICG by the B16F10 cells (Figure 4D). Additionally, as depicted in Figure 4E, the red fluorescence intensity significantly increased with prolonged incubation time. Quantitative analysis using Image J software confirmed a significantly higher average fluorescence intensity of MIL@DOX@ICG at 60 μg/mL compared to 15 μg/mL (42.12 ± 5.51%, $P < 0.001$) and 30 μg/mL (90.69 ± 2.59%, $P < 0.01$), as presented in Figure 4F. The fluorescence intensities at 2, 8, and 24 h were 37.28 ± 7.08%, 64.93 ± 2.04%, and 123.5 ± 10.06%, respectively (Figure 4G), indicating a time-dependent uptake of MIL@DOX@ICG. MIL@DOX@ICG exhibited high affinity to the cell membrane, possibly owing

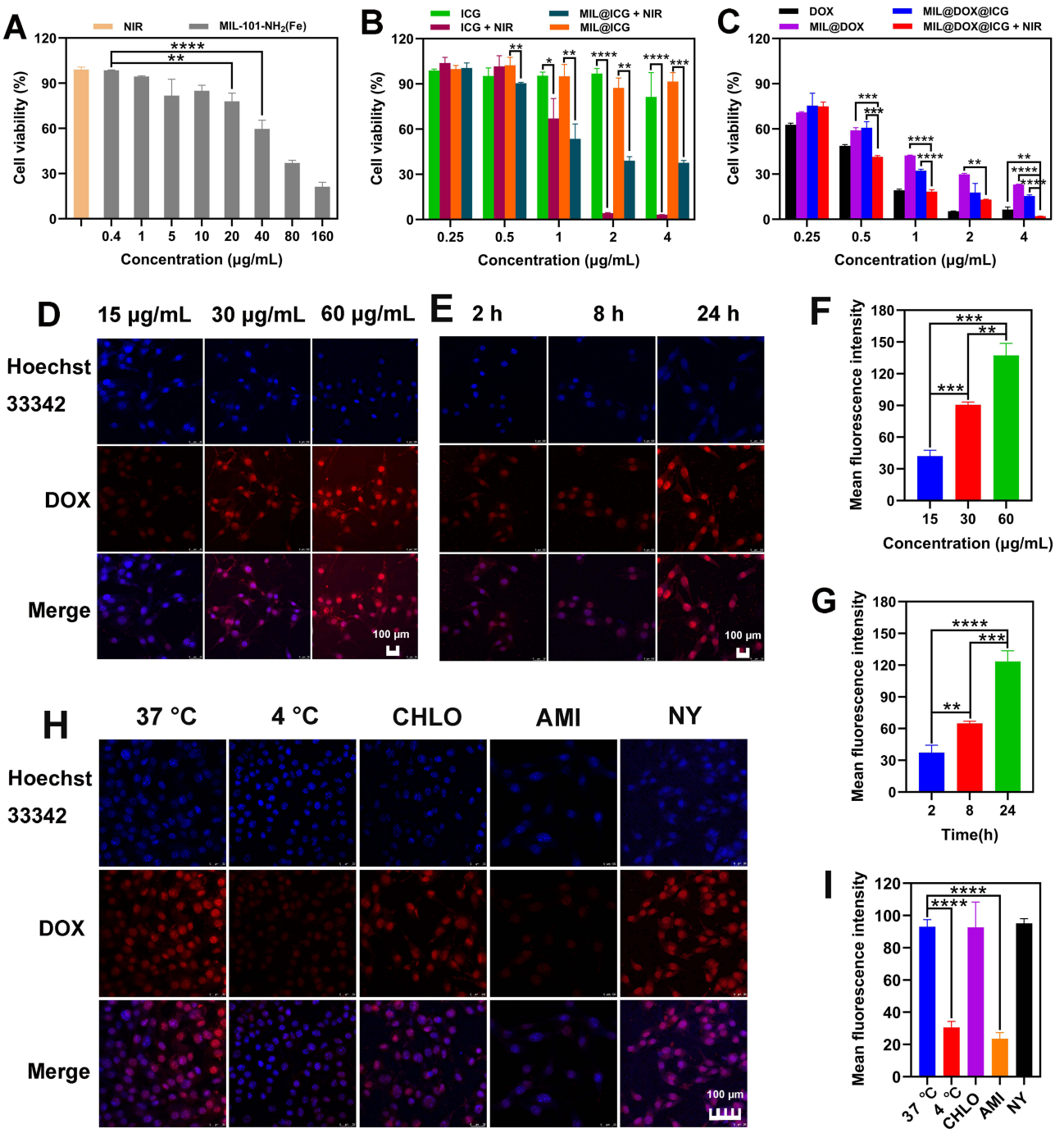

Figure 4 (**A**) Cell viability of B16F10 cells exposed to NIR laser irradiation or incubated with different concentrations of MIL-101-NH_2(Fe). (**B**) Cell viability of B16F10 cells incubated with different concentrations of ICG and MIL@ICG without or with NIR laser irradiation. (**C**) Cell viability of B16F10 cells incubated with DOX, MIL@DOX, and MIL@DOX@ICG without or with NIR laser irradiation. (**D**) Uptake images and (**F**) average fluorescence intensity of B16F10 cells incubated with various concentrations of MIL@DOX@ICG for 8 h. (**E**) Uptake images and (**G**) average fluorescence intensity of B16F10 cells co-incubated with MIL@DOX@ICG at 30 μg/mL for different durations. (**H**) Uptake images and (**I**) average fluorescence intensity of B16F10 cells treatment with MIL@DOX@ICG at 30 μg/mL at 37 °C, 4 °C, and in the presence of various inhibitors. *P < 0.05, **P < 0.01, ***P < 0.001, and ****P < 0.0001.

to interactions between negatively charged nanoparticles and cationic sites on the cell surface, thereby enhancing cellular uptake. These findings confirmed that MIL@DOX@ICG can be efficiently internalized by B16F10 cells in both a concentration- and time-dependent manner, facilitating effective intracellular delivery of the antitumor agents and achieving a pH-responsive release mechanism.

https://doi.org/10.2147/IJN.S502089

To assess the mechanisms underlying cellular uptake, the impacts of low temperature and specific endocytosis inhibitors on the internalization process were investigated. As depicted in Figure 4H and I, a notable reduction in uptake was observed at 4 °C, with an average fluorescence intensity of 30.55 ± 3.76%, significantly lower than that at 37 °C (93.03 ± 4.39%, $P < 0.0001$). This reduction indicated that the uptake of MIL@DOX@ICG by B16F10 cells was energy-dependent, primarily occurring via endocytosis. Three different uptake inhibitors were employed to obstruct specific pathways of endocytosis: CHLO to inhibit clathrin-mediated endocytosis, AMI to block macropinocytosis, and NY to suppress caveolin-mediated endocytosis. The average fluorescence intensities of the groups treated with control, CHLO, AMI, and NY were 93.03 ± 4.39%, 92.61 ± 15.75%, 23.6 ± 3.79%, and 97.98 ± 1.99%, respectively. Notably, the fluorescence intensity in the AMI-treated group was significantly lower than that of the control group ($P < 0.0001$), proving that MIL@DOX@ICG was mainly internalized by B16F10 cells through the macropinocytosis pathway.

Wound Healing Study

The wound healing study was conducted to evaluate the impact of various treatments on cell migration by calculating migration rates. As shown in Figure 5A, NIR laser irradiation and exposure to MIL-101-NH_2(Fe), ICG, or MIL@ICG exhibited no effect on cell migration, affirming the favorable biocompatibility and safety of the laser, carrier, and ICG. Furthermore, the inhibitory capacity on cell migration observed in the ICG + NIR and MIL@ICG + NIR groups, which combined PTT and PDT, was 1.5 times greater than that of the non-irradiated group (Figure 5B). Interestingly, the ICG + NIR and MIL@ICG + NIR groups exhibited comparable abilities to inhibit cell migration. This phenomenon may stem from the limited catalytic efficiency of MIL-101-NH_2(Fe) at this concentration, resulting in a negligible CDT effect consistent with the cytotoxicity outcomes. Upon DOX loading, cell migration was significantly inhibited ($P < 0.0001$), with migration rates falling below 43% (Figure 5C). Remarkably, the migration rate of the MIL@DOX@ICG + NIR group was reduced to merely 15.37 ± 0.58%, reflecting a twofold enhancement in the ability to suppress cell migration compared to the MIL@DOX@ICG group. This improvement can be attributed to the synergistic effects of chemotherapy, PTT, and PDT, indicating the great potential of MIL@DOX@ICG for inhibiting tumor cell migration and metastasis, offering a promising approach for comprehensive cancer therapy.

Cell Cloning Experiment

The relative colony formation number (%) was used to evaluate the impact of various treatments on the colony formation and proliferation ability of B16F10 cells. As presented in Figure 5D and E, treatments including NIR laser irradiation, MIL-101-NH_2(Fe), ICG, ICG + NIR, MIL@ICG, and MIL@ICG + NIR exhibited negligible effects on the cell colony formation rate when compared with the control group. MIL-101-NH_2(Fe) demonstrated no significant cytotoxicity at this concentration, while ICG displayed good biocompatibility without influencing cell division and proliferation. The limited impact observed in the ICG + NIR and MIL@ICG + NIR groups may be attributed to the low concentration of ICG, resulting in insufficient photothermal and photodynamic activities to impede cell division and growth. After encapsulation of DOX, the colony formation and proliferation abilities of tumor cells were markedly suppressed. The colony formation rates of the DOX, MIL@DOX, MIL@DOX@ICG, and MIL@DOX@ICG + NIR groups decreased to 1.24 ± 0.23%, 7.71 ± 1.28%, 7.12 ± 0.57%, and 1.70 ± 0.11%, respectively (Figure 5F). This suppression may be attributed to the direct action of DOX on the DNA of tumor cells, inhibiting their division and growth. Notably, compared with the MIL@DOX and MIL@DOX@ICG groups, MIL@DOX@ICG + NIR exhibited a more pronounced inhibitory effect on colony formation and proliferation of B16F10 cells ($P < 0.001$).

Detection of Intracellular ROS

ROS plays a pivotal role in tumor treatment by inducing oxidative damage to lipids, DNA, RNA, and proteins.[43] Utilizing the ROS-sensitive probe DCFH-DA, which is oxidized by ROS to form green fluorescent 2',7'-dichlorofluorescein (DCF), enables the assessment of intracellular ROS levels. B16F10 cells treated with ICG + NIR and MIL@DOX@ICG + NIR exhibited significant ROS production compared to the control group, with no notable difference in fluorescence intensity between these two groups (Figure 6). In contrast, no obvious ROS production was observed in the ICG and MIL@DOX@ICG groups, indicating that ROS generation primarily arises from ICG production under NIR laser irradiation. Moreover, MIL-101-NH_2(Fe) exhibited negligible ROS generation, possibly due to the low concentrations of GSH and H_2O_2 in tumor cells,

 https://doi.org/10.2147/IJN.S502089

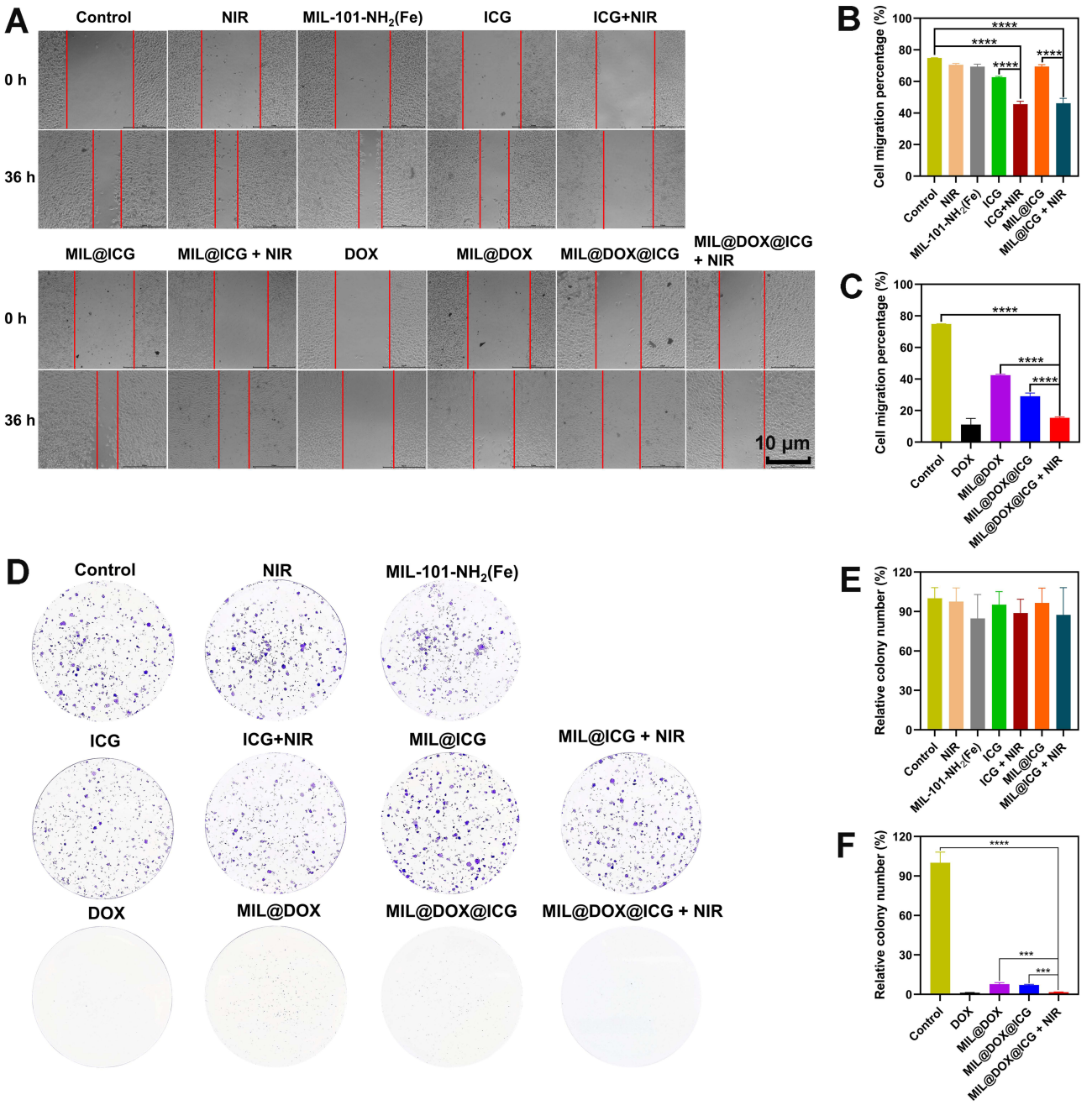

Figure 5 (**A**) Scratch assay images and (**B** and **C**) migration percentage of B16F10 cells treated with different groups. (**D**) Colony formation assay images (**E** and **F**) and relative colony numbers of cells treated with different groups. ***$P < 0.001$, and ****$P < 0.0001$.

causing the subdued Fenton reaction. Another reason for the subdued Fenton reaction may be the low concentration of Fe^{3+} in MIL-101-NH_2(Fe). These observations suggested that MIL@DOX@ICG can effectively exert its PDT effect under the NIR laser irradiation, significantly boosting ROS levels within tumors, thus serving as an effective antitumor strategy.

In vivo Antitumor Effect

Given the excellent cytotoxicity of MIL@DOX@ICG, a melanoma-bearing mouse model was employed for further analysis of the in vivo antitumor effects (Figure 7A). Local hyperthermia is crucial in PTT, accelerating drug release and facilitating both the Fenton reaction and ROS production. After intratumoral injection of MIL@DOX@ICG, the tumor temperature steadily increased under NIR laser irradiation, with the localized high temperature specifically concentrated

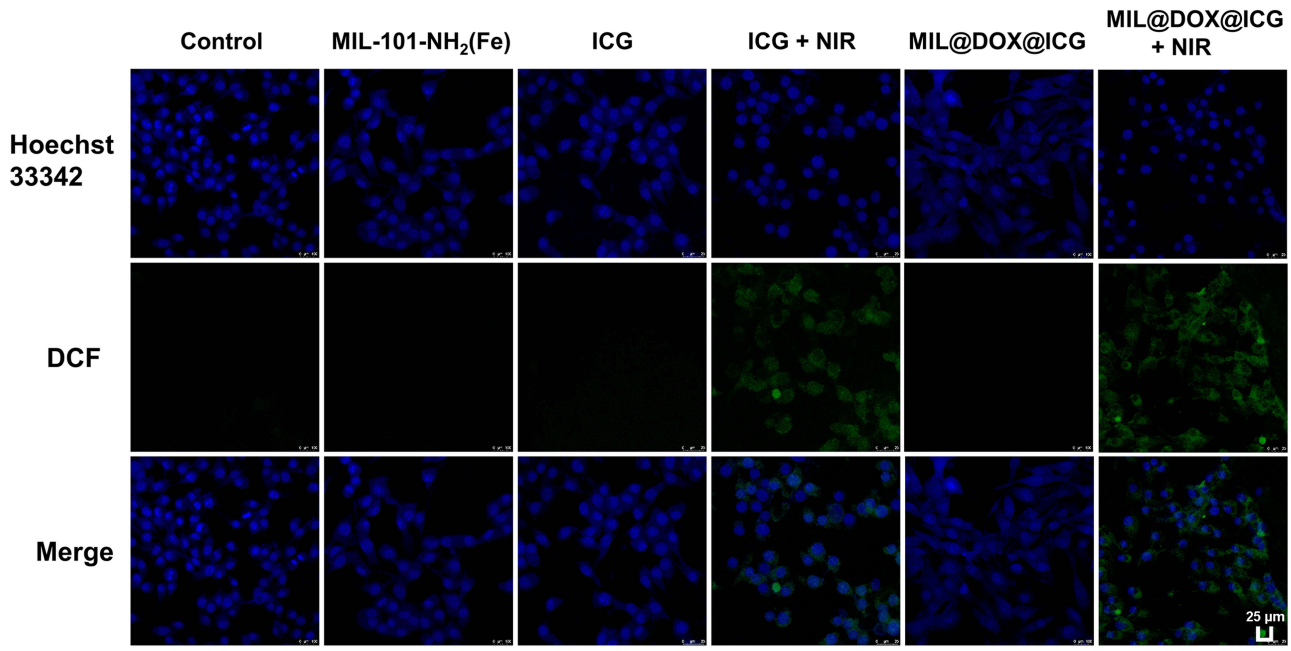

Figure 6 Confocal microscopy images showing intracellular ROS levels in B16F10 cells treated with different conditions for 30 min (DCFH-DA: 10 μM).

in the tumor site. Within the initial minute, the temperature rose to 48.27 ± 3.16 °C, exhibiting an average increment of 15.83 ± 3.94 °C (Figure 7B and C), indicating the outstanding photothermal effect of MIL@DOX@ICG after ICG loading. Over the subsequent 5 min, tumor temperature continued to rise, peaking at 56.03 ± 2.10 °C, surpassing the critical thresholds for cytotoxicity (41.5 °C) and vascular destruction (43 °C). Notably, the temperature achieved by the MIL@DOX@ICG group post-laser irradiation significantly exceeded the threshold for inducing irreversible tumor damage. Thus, through intratumoral administration of MIL@DOX@ICG, the ablative impact on cancer cells induced by PTT can be fully harnessed.

Figure 7D and E depicted the images and average weights of mouse tumors at the end of treatment. Compared with the control group, both the ICG and MIL@ICG groups did not exhibit obvious tumor inhibitory effects, proving their favorable biosafety profiles. With the inclusion of laser irradiation, the combined effects of PTT and PDT via ICG led to local elevation of temperature and toxic ROS within the tumor, thereby restraining tumor growth to a degree in the ICG + NIR and MIL@ICG + NIR groups. The tumor volume in the MIL-101-NH_2(Fe) group exhibited a slight reduction compared to the control group, which was attributed to the presence of Fe^{3+} release from MIL-101-NH_2(Fe) decomposition in tumor tissue. This Fe^{3+} catalyzed the Fenton reaction, generating toxic ROS and inhibiting tumor cell proliferation. After loading with DOX, the tumor volume significantly decreased in both the MIL@DOX and MIL@DOX@ICG groups. This reduction can be attributed to the potent cytotoxicity of DOX, which was released in response to the acidic TME post-intratumoral injection. Notably, the MIL@DOX@ICG + NIR group demonstrated the most pronounced tumor inhibitory effect ($P < 0.05$ versus the control group). The localized hyperthermia induced by NIR laser irradiation not only facilitated the release of DOX and ICG from the carrier but also increased tumor cell permeability, thereby heightening tumor cell sensitivity to chemotherapy drugs. Additionally, the accelerated decomposition of MIL-101-NH_2(Fe) under high local temperatures led to increased Fe^{3+} production, which efficiently catalyzed the Fenton reaction, markedly impeding tumor cell growth under the synergistic effects of chemotherapy, PTT, PDT, and CDT. No significant alterations in body weight were observed across all experimental groups (Figure 7F), indicating that MIL-101@DOX@ICG administration did not induce noticeable side effects during the antitumor therapy in mice.

The H&E staining results of tumor tissues are illustrated in Figure 8A. Tumor cells in the PBS, ICG, and MIL@ICG groups exhibited compact growth, whereas varying degrees of cell shrinkage, sparse arrangement, and nuclear

https://doi.org/10.2147/IJN.S502089

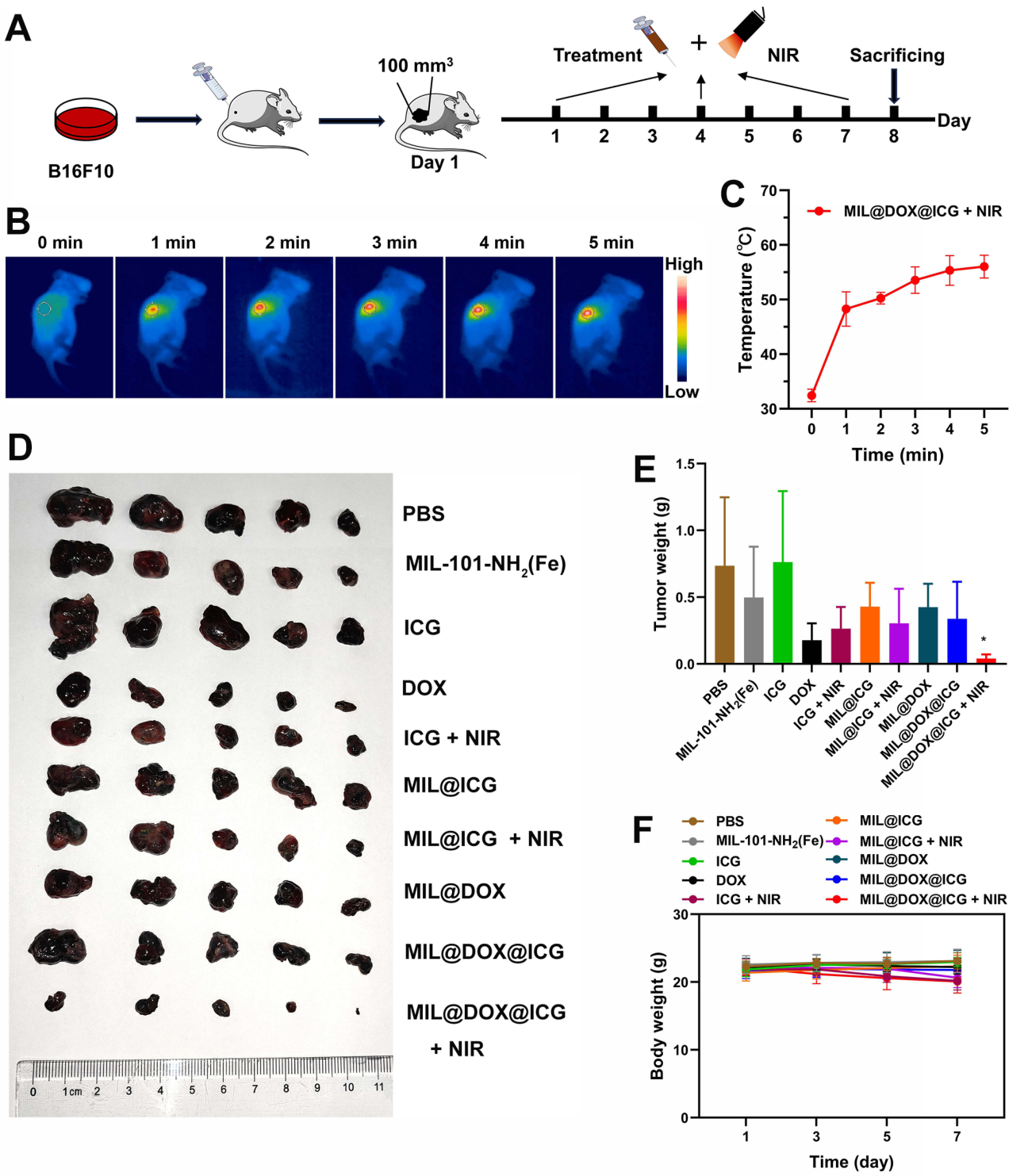

Figure 7 (**A**) Schematic representation of the treatment regimen for B16F10 tumor-bearing mice. (**B**) Infrared thermography images and (**C**) temperature change curve of B16F10 tumor-bearing mice injected with MIL@DOX@ICG and irradiated with NIR laser for 5 min. (**D**) Images of tumors excised from B16F10 tumor-bearing mice after sacrifice. (**E**) Average tumor weight in B16F10 tumor-bearing mice at the end of treatment. *$P < 0.05$. (**F**) The trend of body weight changes in mice during the experiment (n = 5).

destruction were observed in the other treatment groups. Following 808 nm laser irradiation, distinct tumor necrosis and vascular destruction could be clearly observed in the MIL@DOX@ICG + NIR group. Notable morphological alterations of tumor cells were observed, demonstrating typical thermal damage features such as coagulation necrosis, extensive pyknosis, and karyolysis. Moreover, we evaluated tumor tissue proliferation and apoptosis through Ki67 and TUNEL

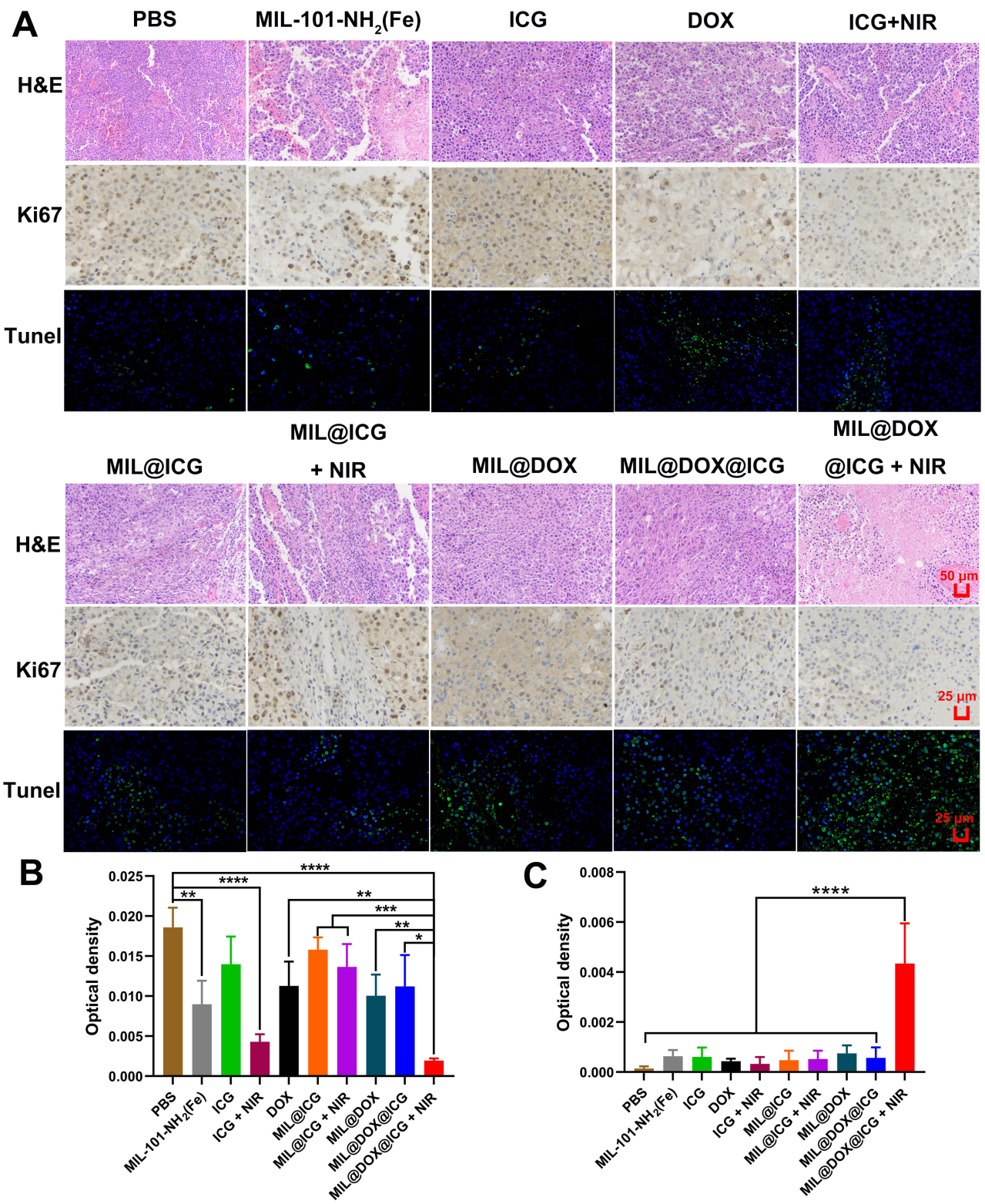

Figure 8 (**A**) Representative images of H&E, Ki67, and TUNEL staining of tumors. Scale bar = 50 μm for H&E and 25 μm for Ki67 and TUNEL. (**B**) Average optical density of Ki67 staining. (**C**) The average optical density of green fluorescence in TUNEL staining. *P < 0.05, **P < 0.01, ***P < 0.001, and ****P < 0.0001.

staining, respectively. Compared with the PBS group, the Ki67 expression levels in MIL-101-NH_2(Fe) and ICG + NIR groups decreased significantly (P < 0.01), suggesting the CDT effect of iron-based nanocarrier and the PDT effect of ICG can inhibit the proliferation of tumor cells (Figure 8A and B). In addition, the expression levels of Ki67 in the

https://doi.org/10.2147/IJN.S502089

MIL@DOX@ICG + NIR group was significantly lower than that in the DOX, MIL@DOX, and MIL@ICG + NIR groups ($P < 0.01$). These results reaffirmed the superior efficacy of combining chemotherapeutic drugs and photosensitizers with NIR laser irradiation therapy over single chemotherapy or dual treatment modalities. TUNEL staining detected green-labeled apoptotic cells, with pronounced green fluorescence observed in the MIL@DOX@ICG + NIR group, significantly higher than the PBS and other treatment groups ($P < 0.05$) (Figure 8A and C). This observation suggested extensive necrosis and severe apoptosis, along with structural damage and nuclear shrinkage, indicating a substantial inhibition effect against tumor cells in the MIL@DOX@ICG + NIR group. These findings further confirmed that under NIR laser irradiation, the synergistic effects of chemotherapy, PTT, PDT, and CDT significantly inhibited tumor cell proliferation and promoted tumor cell apoptosis.

In vivo Safety Evaluation

During the treatment period, mice in each group exhibited normal behavior, with smooth and shiny hair, maintained regular diet and water intake, and no mortality was observed. As depicted in Figure S1, no statistically significant differences were observed in blood cell count parameters among the treatment groups compared to the control group ($P > 0.05$). This suggested that MIL@DOX@ICG did not cause discernible damage or trigger inflammatory reactions in mice after local administration, indicating its favorable biosafety. Furthermore, the safety profile of each group was further evaluated through organ coefficients and histopathological examination. As shown in Figure S2 and S3, no significant differences were noted in organ-to-body and organ-to-brain weight ratios in each treatment group compared to the control group ($P > 0.05$). Additionally, histopathological examinations did not reveal any evidence of cellular necrosis or inflammatory infiltration in any organs, further underscoring the excellent biological safety profile of MIL@DOX@ICG (Figure S4). These findings collectively highlight the potential of employing MIL@DOX@ICG + NIR as an effective and safe antitumor approach.

Conclusion

In this study, we synthesized MIL-101-NH_2(Fe) through a hydrothermal method and successfully loaded DOX and ICG, resulting in the development of the multifunctional MIL@DOX@ICG integrated treatment system. MIL@DOX@ICG demonstrated high drug loading rates and encapsulation efficiencies for both DOX and ICG, as well as robust photothermal stability and ROS generation. In vitro studies revealed that MIL-101-NH_2(Fe) could respond to acidic environments and effectively catalyze H_2O_2 to generate •OH via the Fenton reaction. Cellular experiments confirmed that MIL@DOX@ICG effectively inhibited the migration and clonal proliferation of B16F10 cells under NIR laser irradiation, enhancing therapeutic effects through catalytic ROS production. Furthermore, precise treatment of melanoma cells was achieved via intratumoral injection under 808 nm laser irradiation. Collaborative chemotherapy, CDT, PDT, and PTT exhibited superior tumor treatment effects compared to single treatment methods, significantly suppressing tumor cell division and proliferation while promoting tumor cell apoptosis. Notably, the treatment exhibited no obvious toxicity to normal tissues. Traditional single-modality treatments often exhibit limited efficacy and high recurrence rates due to the complexity of the tumor microenvironment. In contrast, our multifunctional nanoplatform integrates multiple therapeutic strategies, leveraging the acidic and H_2O_2-rich tumor microenvironment to enhance therapeutic outcomes. By achieving precise, responsive drug release and potent antitumor effects, MIL@DOX@ICG addresses key limitations of conventional treatments. These features make MIL@DOX@ICG a versatile and robust platform, offering a significant advancement in melanoma therapy.

Data Sharing Statement

Data will be made available on request.

Funding

This study received support from the Luzhou Municipal People's Government-Southwest Medical University Science and Technology Strategic Cooperation Project (2023LZXNYDJ004), National Natural Science Foundation of China (82104083), Youth Fund of Southwest Medical University (2018-ZRQN-173), Doctor's Fund of Affiliated Hospital of

Southwest Medical University (18109), and Science and Technology Research Special Fund of Sichuan Provincial Administration of Traditional Chinese Medicine (2020JC0133).

Disclosure

The authors declare no conflict of interest in this work.

References

1. Chen Z, Huang Q, Song Y. et al. Cubosomes-assisted transdermal delivery of doxorubicin and indocyanine green for chemo-photothermal combination therapy of melanoma. *Biomed Pharmacother*. 2023;166:115316. doi:10.1016/j.biopha.2023.115316
2. Wang C, Zeng Y, Chen K-F, et al. A self-monitoring microneedle patch for light-controlled synergistic treatment of melanoma. *Bioact Mater*. 2023;27:58–71. doi:10.1016/j.bioactmat.2023.03.016
3. Wu M, Mei T, Lin C, et al. Melanoma cell membrane biomimetic versatile CuS nanoprobes for homologous targeting photoacoustic imaging and photothermal chemotherapy. *ACS Appl Mater Inter*. 2020;12(14):16031–16039. doi:10.1021/acsami.9b23177
4. Li L, Zeng Z, Chen Z, et al. Microenvironment-triggered degradable hydrogel for imaging diagnosis and combined treatment of intraocular choroidal melanoma. *ACS Nano*. 2020;14(11):15403–15416. doi:10.1021/acsnano.0c06000
5. Lu W, Liu W, Hu A, et al. Combinatorial polydopamine-liposome nanoformulation as an effective anti-Breast cancer therapy. *Int J Nanomed*. 2023;18:861–879. doi:10.2147/ijn.S382109
6. Yu J, Wang L, Xie X, et al. Multifunctional nanoparticles codelivering doxorubicin and amorphous calcium carbonate preloaded with indocyanine green for enhanced chemo-photothermal cancer therapy. *Int J Nanomed*. 2023;18:323–337. doi:10.2147/ijn.S394896
7. Zhang Z, Liang X, Yang X, et al. Advances in nanodelivery systems based on metabolism reprogramming strategies for enhanced tumor therapy. *ACS Appl Mater Inter*. 2024;16(6):6689–6708. doi:10.1021/acsami.3c15686
8. Ji HB, Kim CR, Min CH, et al. Fe-containing metal-organic framework with D-penicillamine for cancer-specific hydrogen peroxide generation and enhanced chemodynamic therapy. *Bioeng Transl Med*. 2023;8(3):e10477. doi:10.1002/btm2.10477
9. Li J, Tian H, Zhu F, et al. Amorphous ultra-small Fe-based nanocluster engineered and ICG loaded organo-mesoporous silica for GSH depletion and photothermal-chemodynamic synergistic therapy. *Adv Healthc Mater*. 2022;11(21):e2201986. doi:10.1002/adhm.202201986
10. Cai W, Gao H, Chu C, et al. Engineering phototheranostic nanoscale metal-organic frameworks for multimodal imaging-guided cancer therapy. *ACS Appl Mater Inter*. 2017;9(3):2040–2051. doi:10.1021/acsami.6b11579
11. Liu H, Xu C, Meng M, et al. Metal-organic framework-mediated multifunctional nanoparticles for combined chemo-photothermal therapy and enhanced immunotherapy against colorectal cancer. *Acta Biomater*. 2022;144:132–141. doi:10.1016/j.actbio.2022.03.023
12. Wang Y, Zhang H, Wang J, et al. An engineered design of self-assembly nanomedicine guided by molecular dynamic simulation for photodynamic and hypoxia-directed therapy. *Mol Pharm*. 2023;20(4):2128–2137. doi:10.1021/acs.molpharmaceut.2c01079
13. Zhang L, Lu H, Tang Y, et al. Calcium-peroxide-mediated cascades of oxygen production and glutathione consumption induced efficient photodynamic and photothermal synergistic therapy. *J Mater Chem B*. 2023;11(13):2937–2945. doi:10.1039/d2tb02776c
14. Li X, Pan Y, Zhou J, et al. Hyaluronic acid-modified manganese dioxide-enveloped hollow copper sulfide nanoparticles as a multifunctional system for the co-delivery of chemotherapeutic drugs and photosensitizers for efficient synergistic antitumor treatments. *J Colloid Interf Sci*. 2022;605:296–310. doi:10.1016/j.jcis.2021.07.092
15. Liu Y, Zhang D, Zhang Z, et al. Multifunctional nanoparticles inhibit tumor and tumor-associated macrophages for triple-negative breast cancer therapy. *J Colloid Interf Sci*. 2024;657:598–610. doi:10.1016/j.jcis.2023.11.156
16. Liu J, Sun L, Li L, et al. Synergistic cancer photochemotherapy via layered double hydroxide-based trimodal nanomedicine at very low therapeutic doses. *ACS Appl Mater Inter*. 2021;13(6):7115–7126. doi:10.1021/acsami.0c23143
17. Yang L, Wang K, Guo L, et al. Unveiling the potential of HKUST-1: synthesis, activation, advantages and biomedical applications. *J Mater Chem B*. 2024;12(11):2670–2690. doi:10.1039/d3tb02929h
18. Jo YJ, Gulfam M, Jo SH, et al. Multi-stimuli responsive hydrogels derived from hyaluronic acid for cancer therapy application. *Carbohyd Polym*. 2022;286:119303. doi:10.1016/j.carbpol.2022.119303
19. Li M, Bian X, Chen X, et al. Multifunctional liposome for photoacoustic/ultrasound imaging-guided chemo/photothermal retinoblastoma therapy. *Drug Deliv*. 2022;29(1):519–533. doi:10.1080/10717544.2022.2032876
20. Chen X, Zou J, Zhang K, et al. Photothermal/matrix metalloproteinase-2 dual-responsive gelatin nanoparticles for breast cancer treatment. *Acta Pharm Sin B*. 2021;11(1):271–282. doi:10.1016/j.apsb.2020.08.009
21. Sheng G, Chen Y, Han L, et al. Encapsulation of indocyanine green into cell membrane capsules for photothermal cancer therapy. *Acta Biomater*. 2016;43:251–261. doi:10.1016/j.actbio.2016.07.012
22. Li M, Yang G, Zheng Y, et al. NIR/pH-triggered aptamer-functionalized DNA origami nanovehicle for imaging-guided chemo-phototherapy. *J Nanobiotechnol*. 2023;21(1):186. doi:10.1186/s12951-023-01953-9
23. Wu B, Fu J, Zhou Y, et al. Tailored core-shell dual metal-organic frameworks as a versatile nanomotor for effective synergistic antitumor therapy. *Acta Pharm Sin B*. 2020;10(11):2198–2211. doi:10.1016/j.apsb.2020.07.025
24. Zuo W, Chen W, Liu J, et al. Macrophage-mimic hollow mesoporous Fe-based nanocatalysts for self-amplified chemodynamic therapy and metastasis inhibition via tumor microenvironment remodeling. *ACS Appl Mater Inter*. 2022;14(4):5053–5065. doi:10.1021/acsami.1c22432
25. Ma S, Xie J, Wang L, et al. Hetero-core-shell BiNS-Fe@Fe as a potential theranostic nanoplatform for multimodal imaging-guided simultaneous photothermal-photodynamic and chemodynamic treatment. *ACS Appl Mater Inter*. 2021;13(9):10728–10740. doi:10.1021/acsami.0c21579
26. Mo Z, Pan X, Pan X, et al. MOF(Fe)-derived composites as a unique nanoplatform for chemo-photodynamic tumor therapy. *J Mater Chem B*. 2022;10(42):8760–8770. doi:10.1039/d2tb01691e
27. Shen S, Li L, Li S, et al. Metal-organic frameworks induce autophagy in mouse embryonic fibroblast cells. *Nanoscale*. 2018;10(38):18161–18168. doi:10.1039/c8nr04459g

28. Vinogradov VV, Drozdov AS, Mingabudinova LR, et al. Composites based on heparin and MIL-101(Fe): the drug releasing depot for anticoagulant therapy and advanced medical nanofabrication. *J Mater Chem B*. 2018;6(16):2450–2459. doi:10.1039/c8tb00072g
29. Zhang L, Liu C, Gao Y, et al. ZD2-engineered gold nanostar@metal-organic framework nanoprobes for T_1-weighted magnetic resonance imaging and photothermal therapy specifically toward triple-negative breast cancer. *Adv Healthc Mater*. 2018;7(24):e1801144. doi:10.1002/adhm.201801144
30. Zuo S, Ding Y, Wu L, et al. Revealing the synergistic mechanism of the generation, migration and nearby utilization of reactive oxygen species in FeOCl-MOF yolk-shell reactors. *Water Res*. 2023;231:119631. doi:10.1016/j.watres.2023.119631
31. Liang R, Li F, Chen X, et al. Multimodal imaging-guided strategy for developing ^{177}Lu-labeled metal-organic framework nanomedicine with potential in cancer therapy. *ACS Appl Mater Inter*. 2023;15(39):45713–45724. doi:10.1021/acsami.3c11098
32. Yang Y, Chen Q, Wu J-P, et al. Reduction-responsive codelivery system based on a metal-organic framework for eliciting potent cellular immune response. *ACS Appl Mater Inter*. 2018;10(15):12463–12473. doi:10.1021/acsami.8b01680
33. Cui L, Wang X, Liu Z, et al. Metal-organic framework decorated with glycyrrhetinic acid conjugated chitosan as a pH-responsive nanocarrier for targeted drug delivery. *Int J Biol Macromol*. 2023;240:124370. doi:10.1016/j.ijbiomac.2023.124370
34. Zhao D, Liu J, Zhou Y, et al. Penetrating the blood-brain barrier for targeted treatment of neurotoxicant poisoning by nanosustained-released 2-PAM@VB1-MIL-101-NH_2(Fe). *ACS Appl Mater Inter*. 2023;15(10):12631–12642. doi:10.1021/acsami.2c18929
35. Ma X, Wu Q, Tan L, et al. Chemical chaperone delivered nanoscale metal-organic frameworks as inhibitor of endoplasmic reticulum for enhanced sensitization of thermo-chemo therapy. *Chin Chem Lett*. 2022;33(3):1604–1608. doi:10.1016/j.cclet.2021.09.084
36. Liu Z, Li T, Li N, et al. GSH-induced chemotaxis nanomotors for cancer treatment by ferroptosis strategy. *Sci China Chem*. 2022;65(5):989–1002. doi:10.1007/s11426-021-1208-6
37. Yang L, Shang J, Fan Q, et al. Honokiol-loaded ZIF-90 nanoparticles modified with polydopamine for antitumor therapy. *ACS Appl Nano Mater*. 2024;7(22):25823–25834. doi:10.1021/acsanm.4c04978
38. Zhang Y, Williams GR, Lou J, et al. A new chitosan-based thermosensitive nanoplatform for combined photothermal and chemotherapy. *Int J Biol Macromol*. 2022;223:1356–1367. doi:10.1016/j.ijbiomac.2022.11.068
39. Hong Y, Fang Q, Bai T, et al. Cascade reaction triggering and photothermal AuNPs@MIL MOFs doped intraocular lens for enhanced posterior capsular opacification prevention. *J Nanobiotechnol*. 2023;21(1):134. doi:10.1186/s12951-023-01897-0
40. Song J, Yuan X, Sun M, et al. Oxidation of tetracycline hydrochloride with a photoenhanced MIL-101(Fe)/g-C_3N_4/PMS system: synergetic effects and radical/nonradical pathways. *Ecotox Environ Safe*. 2023;251:114524. doi:10.1016/j.ecoenv.2023.114524
41. Li J, Qiang H, Yang W, et al. Oral insulin delivery by epithelium microenvironment-adaptive nanoparticles. *J Control Release*. 2022;341:31–43. doi:10.1016/j.jconrel.2021.11.020
42. Gao H, Bai Y, Chen L, et al. Self-assembly nanoparticles for overcoming multidrug resistance and imaging-guided chemo-photothermal synergistic cancer therapy. *Int J Nanomed*. 2020;15:809–819. doi:10.2147/ijn.S232449
43. Chen T, Chu Q, Li M, et al. Fe_3O_4@Pt nanoparticles to enable combinational electrodynamic/chemodynamic therapy. *J Nanobiotechnol*. 2021;19(1):206. doi:10.1186/s12951-021-00957-7